Scientific Reports

https://doi.org/10.1038/s41598-026-39995-2

Article in Press

Permeability evolution and microstructural regulation of clay cement grouted body under coupled seepage and stress conditions

Received: 2 December 2025

Accepted: 9 February 2026

Published online: 18 February 2026

Cite this article as: Chai L., Wei Y., Wu K. *et al.* Permeability evolution and microstructural regulation of clay cement grouted body under coupled seepage and stress conditions. *Sci Rep* (2026). https://doi.org/10.1038/s41598-026-39995-2

Lujun Chai, Yaoxiang Wei, Kun Wu & Aiping Cheng

Permeability evolution and microstructural regulation of clay cement grouted body under coupled seepage and stress conditions

Chai Lujun [a, b], Wei Yaoxiang [d*], Wu Kun [a, b], Cheng Aiping [c]

[a] Technology Innovation Center for Groundwater Disaster Prevention and Control Engineering for Metal Mines，Ministry of Natural Resources, Shijiazhuang 050024, China

[b] North China Engineering Investigation Institute Co., Ltd., Shijiazhuang 050024, China

[c] School of Resource and Environmental Engineering, Wuhan University of Science and Technology, Wuhan, Hubei, 430081, China

[d] Guangxi Guoxing Rare Earth Mining Co., Ltd., Chongzuo, Guangxi, 532200, China

* Corresponding author:

Wei Yaoxiang E-mail address: weiyaoxiang1999@163.com

Details of all authors:

Chai Lujun E-mail address: sophyer@126.com

Wei Yaoxiang E-mail address: weiyaoxiang1999@163.com

Wu Kun E-mail address: shuluoye@126.com

Cheng Aiping E-mail address: chengaiping@wust.edu.cn

Abstract: Clay-cement grouted body (CCGB), as a green grouting material, have been widely applied in mine grouting water-blocking technology, and their permeability characteristics are of great significance to the safe mining of mines. Based on this, in this study, CCGB specimens with different cement contents (50%, 70%, 90%) were prepared. Using a rock permeability test system, seepage-stress coupling permeability tests on CCGB were conducted under different cement contents, osmotic pressures, and confining pressures. The permeability characteristics evolution laws of CCGB under different cement contents, osmotic pressures, and confining pressures were clarified; combined with rock microscopic testing, the correlation characteristics among permeability, flow velocity, and porosity of CCGB under different cement contents, osmotic pressures, and confining pressures were investigated; and the permeability characteristics evolution mechanism of CCGB under seepage-stress coupling was revealed. The research results show that:(1) The permeability and microscopic pore structure of CCGB are significantly regulated by cement content: Increasing the cement content from 50% to 70% resulted in a decrease in permeability by $1.81\times10^{-4}\mu m^2$ and a reduction in porosity by 0.076. Increasing the cement content from 70% to 90% resulted in a decrease in permeability by $2.538\times10^{-4}\mu m^2$ and a reduction in porosity by 0.006; (2) Under seepage-stress coupling, the permeability of CCGB is affected by osmotic pressure through the enhancement of seepage erosion: as osmotic pressure increases, fluid erosion is intensified, and porosity, flow velocity, and permeability all increase; (3) Under seepage-stress coupling, seepage in CCGB is inhibited by confining pressure through the enhancement of volume compression: with the increase of confining pressure, the volume shrinkage and seepage inhibition effects of CCGB are strengthened, and porosity, seepage

velocity, and permeability all decrease; (4) Under seepage-stress coupling, the permeability characteristics evolution of CCGB is dominated by the competitive balance between erosion effect and compaction effect, and microscopic pore structure and mineral composition are the key regulatory factors. The research results can provide theoretical guidance for the production practice of green grouting engineering.

Keywords: Seepage-stress coupling; Permeability characteristics; Mine curtain grouting

List of symbols

CCGB	Clay-Cement Grouted Body
XRD	X-ray Diffraction
XRF	X-ray Fluorescence
SSCP	Seepage-Stress Coupled Permeability
NMR	Nuclear Magnetic Resonance
SEM	Surface Electron Microscope

1 Introduction

Many mines in China are plagued by challenging hydrogeological predicaments. Characterized by complex hydrogeological conditions and abundant water storage in aquifers, these mines experience persistently high-water inflow in their pits [1]. During mine production and construction, the exposure of water heads carries a high risk of triggering sudden water gushing, which can lead to the rapid submersion of mine shafts or mining areas [2]. This not only inflicts heavy economic losses on the nation and society but also results in casualties, thereby severely impeding the safe and stable development of the mining industry. A grouting curtain is defined as a continuous structural body with a certain degree of strength and impermeability, formed within a specific range through a series of processes—including diffusion, filling, and cementation—by injecting specialized grout materials into the stratum. Acting as a barrier, it blocks or restricts the flow paths of fluids such as groundwater. As the core component of the grouting curtain, the water-blocking efficiency and permeability of the set grout are directly critical to the safe production of water-rich mines [3-8].

The permeability of rock is influenced by a variety of factors, including specimen size, fluid properties, pressure gradient, ambient

temperature, saturation, and physicochemical reactions [9-13]. In recent years, scholars at home and abroad have conducted extensive experimental studies on the testing of rock permeability. Liu et al. [14] found that sandstone exhibits brittle tensile-shear failure, dilatancy decays exponentially with confining pressure, and a dual-stage permeability model captures nonlinear evolution driven by pore compaction and crack propagation. Zhang et al. [15] revealed that confining pressure and fracture surface roughness negatively correlate with permeability, while fracture width and fracture geometry positively correlate with permeability; with confining pressure being the most influential. Ma [16-17], and Wu et al. [18] conducted experimental studies on the seepage characteristics of fractured rock masses, and obtained the time-dependent law governing the variable-mass seepage characteristics of fractured rock masses. Wang et al. [19] demonstrated through their research that permeability decreases with increasing load before the rock reaches its peak strength. Nicksiar et al. [20] showed that for rock samples with low permeability, three compression loading stages—crack initiation, unstable crack propagation, and peak strength—can generally be identified. They proposed using the circumferential strain response method to determine the stress at the point of crack

initiation, which serves as the cracking point for the excavation and unloading of brittle rock masses. Shu et al. [21] studied the seepage characteristics of granite with prefabricated long fractures at temperatures ranging from room temperature to 200℃ through experimental work. They found that the permeability of fractured granite gradually decreases under the action of long-term high-temperature fluid flow, and this change in permeability is irreversible. Zhang et al. [22] performed long-term permeability tests and established a coupling model to describe the damage distribution of fractures, thereby revealing the relationship between thermal stress and the evolution of fracture permeability. Yin et al. [23] analyzed the evolution process of nonlinear seepage characteristics of rock masses under different confining pressures and water inlet pressure conditions, based on split rough single-fracture specimens. Sun et al. [24] constructed a fracture network model of the rock mass in the study area, and combined it with numerical simulation methods to explore the influence of fracture geometric characteristics on nonlinear seepage characteristics. Their work further revealed the regulatory law of fracture network connectivity on seepage anisotropy. Zhu [25] developed a cost-effective true triaxial system for fracture stress-seepage coupling;

revealed that low σ_3 amplifies ε_3 growth and σ_1 sensitivity, that higher σ_3 diminishes their influence, and that principal stresses negatively affect strain and flow. Yao et al. [26] investigates high-strength self-compacting concrete-based expansive grout, revealed a four-phase expansion mechanism driven by $Ca(OH)_2$ crystals, optimal cement content at 58.8% for single free surface expansion rate, S-shaped curve effects of expansion agent on single free surface expansion rate, lateral expansion pressure, and confirming engineering viability for rock reinforcement through macro-micro analysis of volume, pressure evolution. Grouted stone bodies are core to grouting curtains, forming continuous impermeable barriers by filling water-conducting fractures and pores in rock masses and cementing with surrounding rocks, thus blocking groundwater seepage paths. Scholars have focused on the permeability and evolution mechanism of grouted stone bodies, exploring their dynamic permeability laws via field tests, laboratory measurements, and numerical simulations based on multi-field coupling theory [27-30].

In summary, while extensive research has been conducted on the permeability characteristics of rocks and rock masses, studies on the permeability of CCGB are limited. Particularly, in-depth

investigation into the evolution mechanism of clay permeability under the coupling of osmotic pressure and confining pressure is lacking.

Accordingly, this study prepared CCGB specimens with different cement contents (50%, 70%, 90%). Using a rock permeability test system, seepage-stress coupling permeability tests were performed under varying cement contents, osmotic pressures, and confining pressures to clarify the evolution laws of CCGB permeability characteristics under these conditions. Combined with rock microscopic tests, the correlations among permeability, flow velocity, and porosity of CCGB under different conditions were explored, ultimately revealing the evolution mechanism of CCGB permeability characteristics under seepage-stress coupling.

2 Materials and method

2.1 Raw material analysis

In this test, mineral red clay was used as the material, 32.5# ordinary Portland cement was adopted as the cementitious material, and the water used in the test was tap water from the laboratory. The particle size distribution of clay particles is shown in Fig.1(a), and that of cement particles is shown in Fig.1(b). Fig.2(a) presents the X-ray diffraction (XRD) results of the clay, and Fig.2(b) presents the XRD results of the cement. The results show that the main mineral components of the clay are kaolinite, quartz and calcite; the main mineral phases of the cement are calcium silicate, quartz and gypsum. The red clay exhibits a particle size distribution with a Uniformity Coefficient of 16.57 and Coefficient of Curvature of 1.15, indicating well-graded properties. Its relatively uniform distribution and appropriate max-min particle size gap confirm suitability as CCGB.

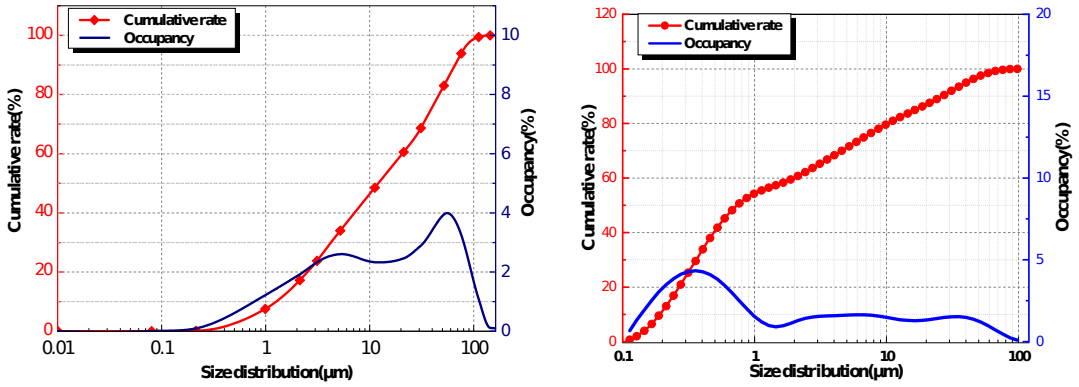

（a）red clay　　（b）cement

Fig. 1 Raw material particle size distribution curve

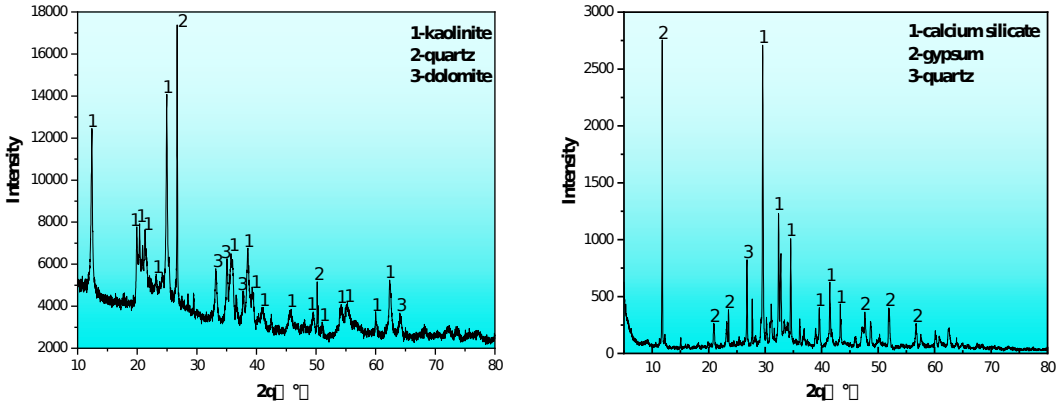

（a）red clay （b）cement

Fig. 2 X-ray diff diffraction pattern

Table 1 and Table 2 show the X-ray fluorescence (XRF) results of the clay and cement. The main elements in the red clay are Si, Al, and Fe, with the main oxides being SiO_2, Al_2O_3, and Fe_2O_3 (totaling 95.9%), in addition to small amounts of oxides of Ti, K, and Ca. The main chemical elements in the cement are Ca, Si, and Al, with the main oxides being CaO, SiO_2, and Al_2O_3 (totaling 72.9%), along with small amounts of oxides of Fe, Mg, and Al. High Al_2O_3, SiO_2 content in clay undergoes a pozzolanic reaction with the cement hydration product $Ca(OH)_2$, generating C-S-H gels. These gels effectively fill the pores of the clay-cement mixture, reducing its permeability coefficient. This clay-cement system provides a reliable basis for constructing low-permeability barrier bodies through the optimization of compactness and leaching resistance.

Table 1 Chemical composition of clay

composition	Si	Al	Fe	Ti	K	Ca	Cl	Zr

Proportion / %	22.37	20.13	13.09	1.09	1.01	0.80	0.13	0.10
composition	SiO_2	Al_2O_3	Fe_2O_3	TiO_2	K_2O	CaO	Cl	ZrO_2
Proportion / %	43.80	35.62	16.47	1.63	1.10	1.00	0.12	0.11

Table 2 Elemental composition of cement

composition	Ca	Si	Al	Fe	Mg	S	K	Na
Proportion / %	32.50	8.84	4.09	2.09	1.18	1.17	0.68	0.15
composition	CaO	SiO_2	Al_2O_3	Fe_2O_3	MgO	SO_3	K_2O	Na_2O
Proportion / %	45.44	18.91	8.52	2.98	1.85	2.93	0.82	0.19

2.2 Experimental procedure

In this experiment, standard cylindrical molds with a diameter (Φ) of 50 mm and a height (H) of 100 mm were used to prepare CCGB samples with a cement content of 50%, 70%, and 90% respectively, and a mass concentration of 56%. The samples were left to stand for 24 hours for demolding, and then cured in a YH-40B standard curing chamber for 28 days. Finally, macroscopic seepage-stress coupling permeability tests and microstructural tests were carried out respectively. The sample numbers and test conditions are listed in Table 3. The preparation and test process of the clay-stone bodies are shown in Fig.4, including seepage-stress coupled permeability

(SSCP), XRD, nuclear magnetic resonance (NMR), and surface electron microscope (SEM) tests.

Table 3 Experimental scheme

Number	cement content /%	seepage pressure /MPa	confining pressure /MPa
1	50	2	2.5
2	70	2	2.5
3	90	2	2.5
4	70	1.5	2.5
5	70	1	2.5
6	70	1.5	2
7	70	1.5	3

SSCP test was an important method for obtaining the macroscopic permeability properties (permeability, porosity, flow velocity) of clay-stone bodies. After the clay-stone bodies reach a 28-day curing age, the SSCP tests were conducted on the clay-stone samples using a rock seepage-stress coupling permeability testing machine. The SSCP tests adopt a hydraulic control mechanism with a loading rate of 0.02 MPa/s.

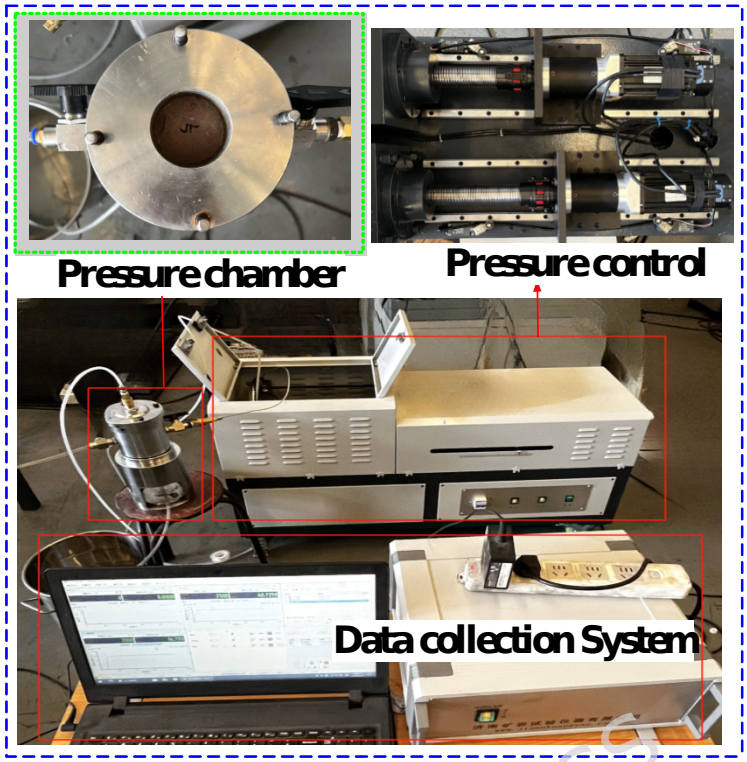

Fig.3. The test system of SSCP

The SSCP tests were conducted using a rock permeability testing system (as illustrated in Fig.3). This experimental system consists of a rock triaxial cell, a confining and pore pressure control system, and a data acquisition and processing system. It allows for the independent or synchronous loading of confining and pore pressures. Furthermore, the system enables real-time recording of fluid flux and the circumferential/volumetric deformation of the specimen, facilitating the monitoring of porosity and permeability evolution throughout the testing process. The experimental procedure for this permeability system primarily includes the following steps:

(1) **Specimen Installation**: The specimen is placed into the rock triaxial cell, ensuring that the base of the specimen is in flush

contact with the bottom of the chamber, followed by the installation of the top cap.

(2) **Fluid Replenishment**: The hydraulic reservoirs of the confining and pore pressure control systems are filled with a specified volume of testing fluid.

(3) **Piping Connection**: The pressure lines of the rock triaxial cell are coupled to the pressure control system to establish the pathways for confining and pore pressures.

(4) **Loading Configuration**: The target values for confining and pore pressures are prescribed. Upon configuration, the loading process is initiated; typically, the confining pressure is applied first and allowed to stabilize before the pore pressure is loaded.

(5) **Loading and Monitoring**: The displacements (volume changes) associated with the pore and confining pressures are monitored. Once these displacements have stabilized, the readings are tared (zeroed). The specified pressure conditions are maintained for a sufficient duration to ensure adequate seepage before terminating the experiment.

(6) **Data Processing**: Time-series data for pore and confining pressure displacements are exported from the computer system to calculate the real-time evolution of permeability, volumetric strain, and porosity during the permeability test.

NMR test was conducted to obtain the initial porosity of the CCGB and the changes in internal pore size after the SSCP test. The CCGB was placed in a vacuum saturation device for 48 hours to allow water to fill its pores, and then transferred to a rock low-field nuclear magnetic resonance instrument manufactured by Niumai Company. When the water-saturated rock is placed in a magnetic field, it exhibits certain relaxation characteristics. By measuring parameters such as relaxation time, the instrument can invert information including the pore size distribution and porosity of the grouted body.

After the NMR test, a WAW-100kN microcomputer-controlled electro-hydraulic servo universal testing machine was used to perform uniaxial crushing on the CCGB specimens. The sample fragments were immersed in pure ethanol for three days and then dried in an oven at 40℃ until a constant mass was achieved. Immersion in pure ethanol was intended to prevent further changes in cement hydration products. These crushed samples, which were not polished and retained their natural fracture surfaces, were prepared for subsequent microstructural testing.

XRD test was mainly used to analyze the phase composition, particle size, and crystallinity of the CCGB by comparing with standard diffraction patterns. 10g of dried sample and 4g of ethanol were ground in a mortar for approximately 5 minutes to obtain fine particles with a particle size less than 74μm (below 200 mesh).

Subsequently, the powder sample was air-dried naturally and bagged, after which the XRD test was performed on the powder sample using a Japanese Rigaku SmartLab SE X-ray diffractometer. The scanning speed was 10°/min, and the scanning range (2θ angle) was from 10°to 80°.

SEM test was used to characterize the microstructure of CCGB after seepage-stress coupling effect. Due to the porous nature and poor electrical conductivity of CCGB samples, direct SEM testing is not feasible. To enhance the electrical conductivity of the samples, 5g of crushed samples need to be placed on a small copper plate, fixed with conductive adhesive, and their surfaces subjected to gold sputtering coating treatment using an EMITECH K550X instrument. The gold-sputtered samples are then sent to a Czech TESCAN MIRA LMS scanning electron microscope for vacuum extraction, and the surface micromorphology of the samples is observed under an accelerating voltage of 10~15kV with a magnification of 1000~10000×.

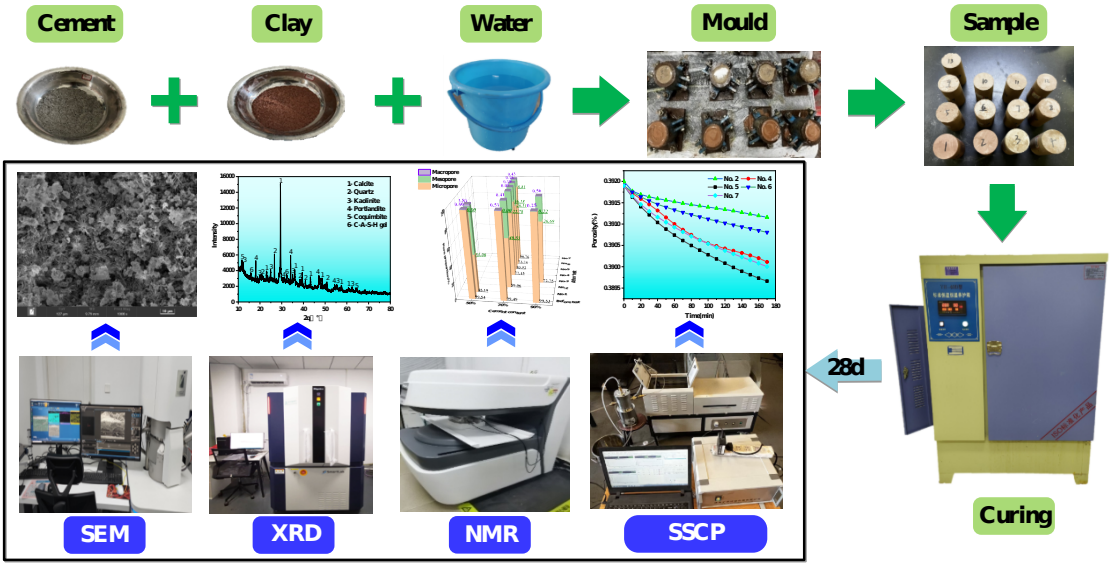

Fig.4. The preparation and test process of CCGB

3 Results

3.1 SSCP

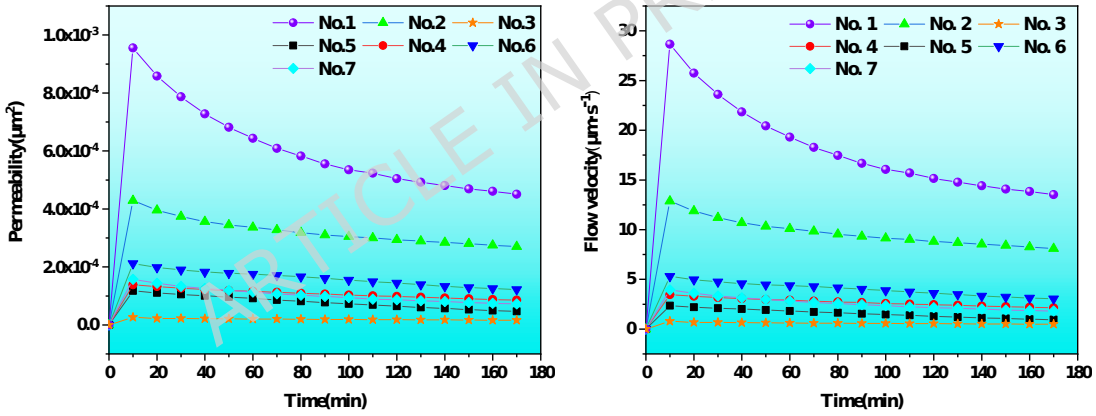

(a) Permeability (b) Flow velocity

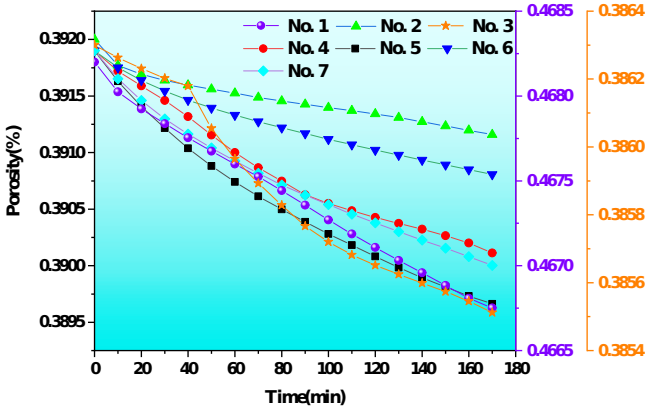

(c) Porosity

Fig.5. SSCP test results of CCGB.

This paper mainly characterizes the seepage characteristics of cemented tailings under seepage-stress coupling using three parameters: porosity, flow velocity, and permeability. The calculation methods for each characterization parameter are as follows.

(1) Porosity Calculation

The initial porosity of the specimen is obtained by nuclear magnetic resonance. The specific calculation process of the specimen's porosity during the test is as follows:

Considering the volume strain of the specimen, the change in porosity during the seepage test is calculated by monitoring the change in the volume strain of the cemented tailings, which can be expressed as:

$$\varphi_i = 1 - \frac{1 - \varphi_0}{1 + \varepsilon_{Vi}} \quad (1)$$

where φ_i is the porosity of the specimen at time t_i; φ_0 is the initial porosity of the specimen; ε_{Vi} is the volume strain at time t_i, which can be calculated by the confining pressure displacement and the diameter of the hydraulic pipeline, and is obtained by the following formula:

$$\varepsilon_V = \frac{\pi r_2^2 L_2}{V} \tag{2}$$

where r_2 is the radius of the hydraulic chamber corresponding to the confining pressure, L_2 is the confining pressure displacement, and V is the initial volume of the specimen.

(2) Flow Velocity Calculation

The seepage velocity of the specimen can be calculated based on the seepage flow collected by the test system. The seepage flow Q is calculated by the osmotic pressure displacement and the diameter of the hydraulic pipeline:

$$Q = \pi r_1^2 L_1 \tag{3}$$

where r_1 is the radius of the hydraulic chamber corresponding to the osmotic pressure, and L_1 is the osmotic pressure displacement.

$$q_i = \frac{4Q_i}{\pi d^2} \tag{4}$$

where Q_i is the fluid flow collected at the i-th time; q_i is the average flow velocity at the i-th time; d is the diameter of the specimen.

(3) Permeability Calculation

According to Darcy's law:

$$-\nabla P = \frac{\mu}{k} q_i \tag{5}$$

where $-\nabla P$ is the hydraulic pressure gradient, determined by the ratio of the water pressure difference between the inlet and outlet of the seepage to the height of the specimen; μ is the dynamic viscosity of water; k is the permeability.

Substituting Equation (4) into Equation 5), the permeability of the specimen can be obtained as:

$$k = \frac{4Q_i \mu h}{\pi d^2 (P_{in} - P_{out})} \tag{6}$$

where P_{in} and P_{out} are the water pressures at the inlet and outlet ends of the specimen, respectively.

Fig. 5 shows the evolution process of seepage characteristics of CCGB under seepage-stress coupling effect. The sample has been subjected to saturation treatment by vacuum saturation method before conducting the seepage test. The permeability and porosity of CCGB decrease with the increase of cement content: the permeability decreases from 4.51×10^{-4} μm² at 50% cement content to 1.62×10^{-5} μm² at 90% cement content; the porosity decreases from 46.8% at 50% cement content to 38.6% at 90% cement content. At the initial stage of seepage loading, i.e., within the time period of

0~10 min, the porosity of the specimen shows a trend of rapid decrease, and at the same time, the flow velocity and permeability increase rapidly and reach their respective peaks. During the period of 10~100 min of the permeability test, the porosity of the specimen continues to decrease with time, but the decreasing rate gradually slows down, indicating that the decreasing process of porosity gradually slows down with the continuous action of confining pressure. Meanwhile, the flow velocity and permeability show a similar change process. After reaching the peak, they also begin to decrease with time, and the decreasing rate also slows down gradually, which is consistent with the decreasing process of porosity. This indicates that there is a close correlation between the porosity, permeability, and flow velocity of CCGB. In addition, after 180 minutes of the seepage experiment, the permeability and flow velocity tend to stabilize, however, the porosity continues to decrease. It may be due to a decrease in pore volume, but the reduction is in ineffective pores such as isolated pores, while retaining and optimizing effective pores (pores with good connectivity and unobstructed channels), resulting in a stable permeability and flow velocity.

According to the results, it can be concluded that cement content classification for permeability control. (a) High-barrier applications (e.g., adjacent to aquifers). A cement content of 90% is recommended to form a dense, erosion-resistant matrix. This formulation effectively suppresses initial permeability peaks and ensures environmental safety. (b) Moderate permeability control. A 70% cement content provides optimal balance between material economy and structural stability, suitable for intermediate hydraulic demands. (c) Low-risk zones with minimal hydrostatic pressure. A 50% cement content offers an economical solution for non-critical areas. Caution: This mix exhibits higher initial porosity, leading to significantly elevated permeability peaks. It is strictly prohibited in high-risk hydrogeological contexts and applicable only to short-term stress conditions.

3.2 NMR

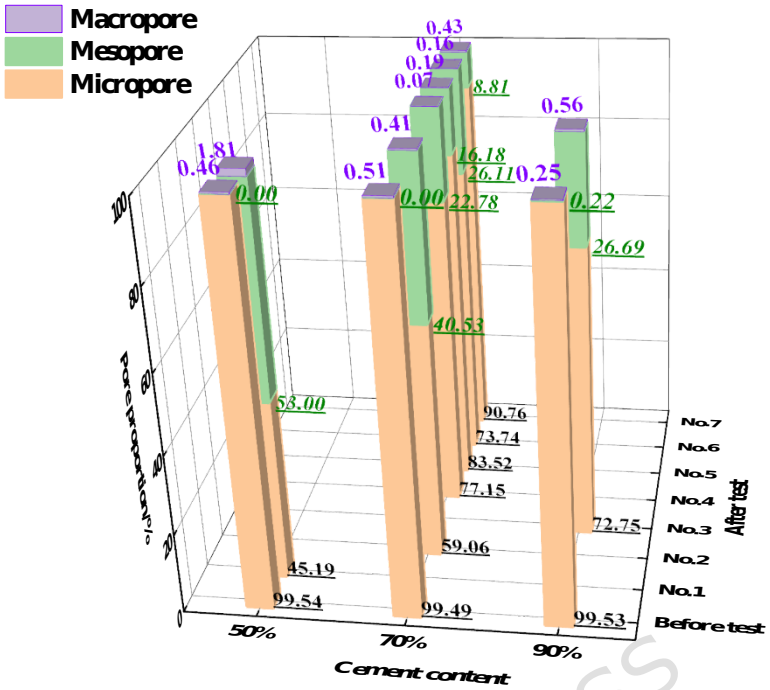

Fig.6. NMR test results of CCGB.

Based on the analysis of NMR tests, the calculated pore sizes of each CCGB specimen were classified into three categories: micropores, mesopores, and macropores. The classification criteria are as follows: micropores < 0.1 μm, 0.1 μm ≤ mesopores ≤ 1 μm, and macropores > 1 μm [31]. The pore proportions of CCGB under different conditions derived from this classification are shown in Fig. 6.

As can be seen from the figure, before the permeability test, there is no significant difference in the pore proportions among CCGB specimens with different cement contents: the proportion of micropores is around 99.5% for all specimens, while the proportion of macropores decreases from 0.46% (at 50% cement content) to

0.25% (at 90% cement content). In addition, only the CCGB specimen with a cement content of 90% contains mesopores, accounting for 0.22%. This phenomenon is attributed to the fact that CCGB specimens with a higher cement content generate more hydration products and have a denser internal structure, which hinders the development of some mesopores into macropores, resulting in the persistence of some mesopores.

After the permeability test, due to the seepage erosion during the test, CCGB exhibits a phenomenon where the proportion of micropores decreases while the proportion of mesopores increases. Specifically, the proportion of micropores decreases by an average of 23.32%, and the proportion of mesopores increases by an average of 23.51%, the magnitude of these two changes is comparable. This indicates that seepage erosion causes micropores to develop into mesopores, which may further connect to form seepage channels. It should be noted that although the proportion of mesopores increases, the total number of pores and the porosity of CCGB consistently decrease, as shown in Fig. 5(c).

3.3 XRD

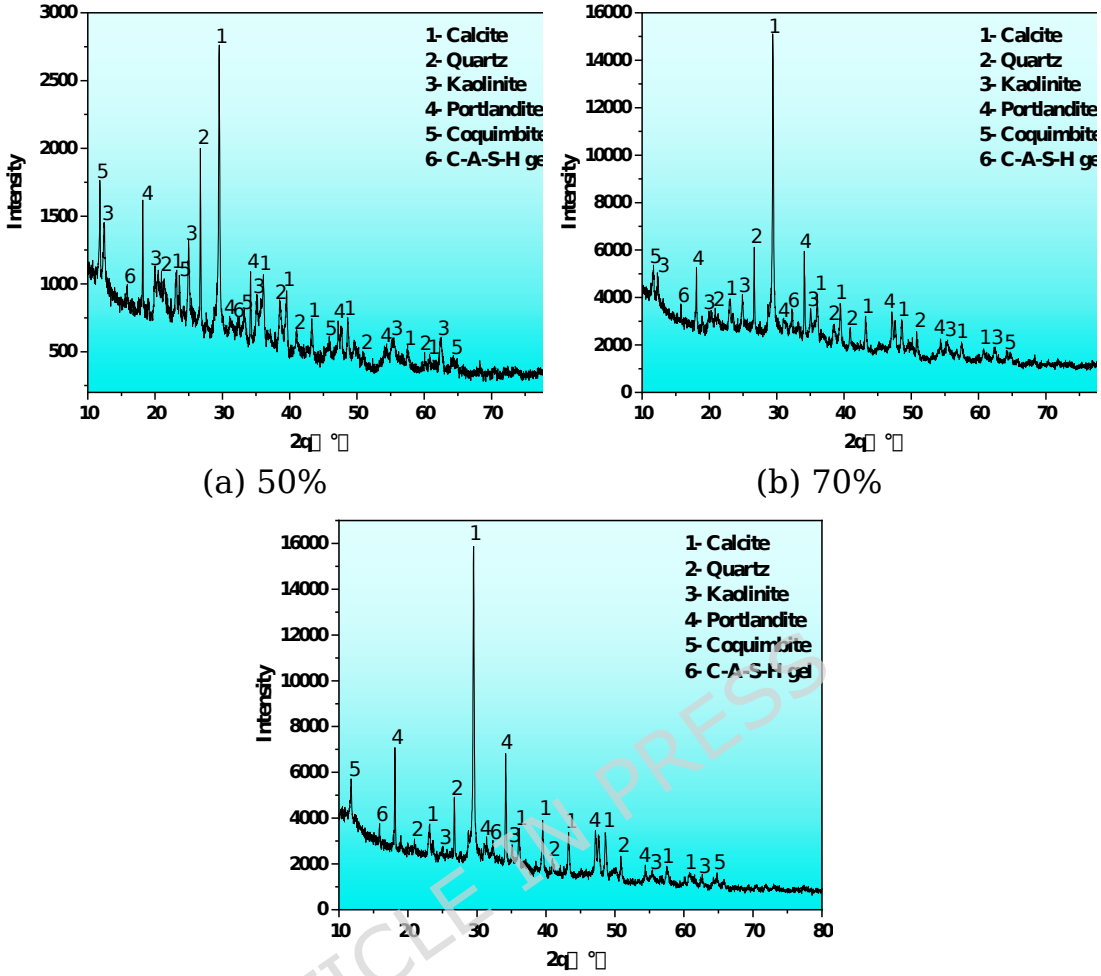

(a) 50% (b) 70%

(c) 90%

Fig.7. XRD results of CCGB at different cement content.

Fig.7 shows the XRD results of CCGB with different cement contents. Based on the intensities of different diffraction peaks, it can be observed that the phase composition of CCGB is consistent across specimens with different cement contents, mainly including calcite, quartz, melanterite, kaolinite, and C-A-S-H gel. The differences in their peak intensities are primarily caused by the variation in cement content.

As shown in Table 4, the diffraction intensity of each phase exhibits a certain regularity with the increase of cement content, which indirectly reflects the relationship between the content of each phase and cement content. Among them, calcite has the highest content, followed by quartz, kaolinite, and calcium hydroxide, while melanterite and silicoaluminate gel have the lowest contents.

With the increase of cement content, the diffraction peak intensities of calcite and calcium hydroxide in CCGB increase significantly: the former increases from 8762 (at 50% cement content) to 37615 (at 90% cement content), and the latter rises from 4251 (at 50% cement content) to 22505 (at 90% cement content). In addition, the content of silicoaluminate gel also increases significantly with the increase of cement content.

The mineral composition of CCGB is simple, mainly consisting of cement hydration products and clay-phase minerals inherent in the clay itself. The calcium hydroxide and silicoaluminate gel generated during the hydration process can fill the pores between particles, making the pore structure of CCGB more refined and uniform, and reducing its permeability. This explains why the porosity of CCGB decreases with the increase of cement content.

Table 4 Mineral composition of CCGB with different cement contents

	calcite	quartz	melanteri	kaolinite	calcium	C-A-S-H

cement content			te		hydroxide	gel
	diffraction intensity	diffraction intensity	diffraction intensity	diffraction intensity	diffraction intensity	diffraction intensity
50%	8762	5623	4728	6037	4251	1750
70%	37171	17842	7125	20240	20003	7253
90%	37615	12592	7334	8892	22505	6791

3.4 SEM

ImageJ software was used to perform pore extraction on CCGB samples under different cement contents and osmotic pressures. First, the SEM images were preprocessed using ImageJ software, including noise reduction and contrast enhancement, to improve image quality. Subsequently, the pore regions were accurately extracted by segmenting the images using an adaptive thresholding segmentation algorithm. The pore extraction process is shown in Fig. 8.

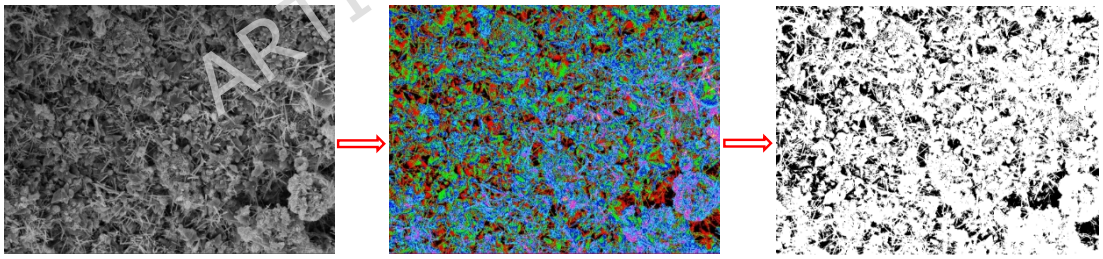

Fig.8. Pore extraction schematic diagram of CCGB section

Fig. 9 shows the SEM images of CCGB with different cement contents before and after the permeability testing. Among them, samples a, c, and e are CCGB with different cement contents that have not undergone SSCP testing, while samples b, d, and f are CCGB with different cement contents that have undergone SSCP

testing, corresponding to samples 1-3 in Table 3. Table 5 presents the micropore information obtained from image processing. Although porosity values differ due to the principles of the measurement methods (SEM tests is surface imaging vs. NMR tests is volumetric analysis), the porosity trends are consistent across both methods, providing mutual verification. Combined analysis reveals that with the increase of cement content, the number and size of micropores within CCGB generally decrease, and the pore connectivity also decreases. Specifically, the number of pores in CCGB decreases from 4614 (at 50% cement content) to 3328 (at 90% cement content); the pore area decreases from 933.5 to 671.2; and the pore proportion decreases from 8.26% to 5.12%. The pore information of CCGB after the permeability test shows the same variation law.

In addition, analysis of the SEM pore images of CCGB after seepage-stress coupling effect indicates that the pores of CCGB with various cement contents all decrease after the coupling effect. For CCGB with 50% cement content, the number of pores and pore proportion decrease from 4614 and 8.26% to 2513 and 7.57% respectively after seepage-stress coupling; for that with 70% cement content, the number of pores and pore proportion decrease from 3817 and 6.22% to 1498 and 4.58% respectively; and for that with

90% cement content, the number of pores and pore proportion decrease from 3328 and 5.12% to 1523 and 2.76% respectively. This indicates that under seepage-stress coupling effect, the microscopic pore structure of CCGB mainly shows a state of closure and shrinkage, the internal structure becomes denser, and the compaction effect of confining pressure is more significant.

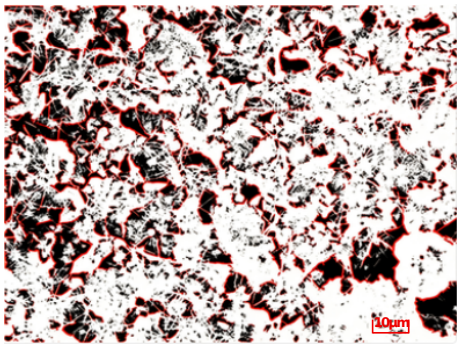

(a)

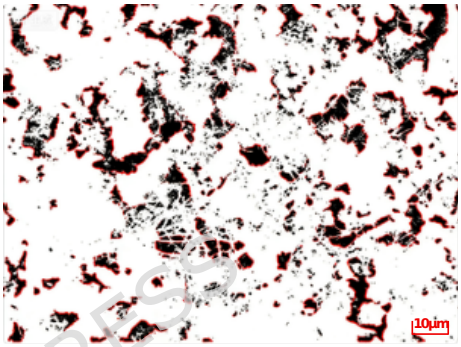

(b)

(1) 50%

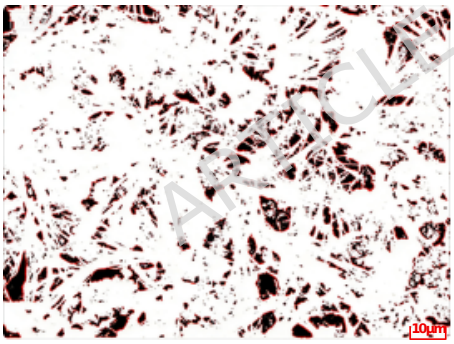

(c)

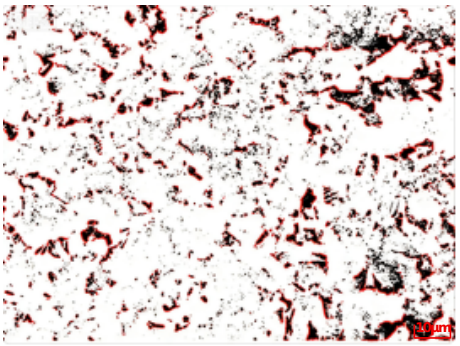

(d)

(2) 70%

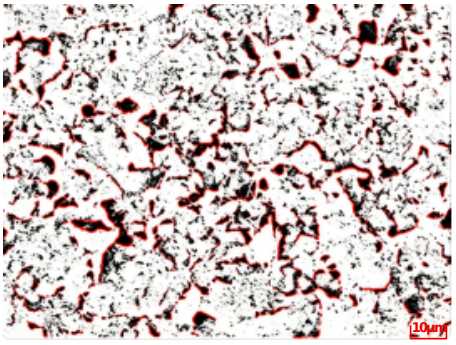

(e)

(f)

(3) 90%

Fig.9. SEM-Based Microscopic Pore Images of CCGB (Left: before the permeability test; Right: after the permeability test)

Table 5 SEM-Based Microscopic Pore Information of CCGB

Number	Osmotic pressure/ MPa	Confining pressure/ MPa	Cement content /%	Pore quantity	Pore area/μm^2	Proportion /%
a	-	-	50	4614	1014.5	8.26
c	-	-	70	3817	836.2	6.22
e	-	-	90	3328	671.2	5.12
b	2	2.5	50	2513	950.5	7.57
d	2	2.5	70	1498	558.3	4.58
f	2	2.5	90	1523	261.9	2.76

4 Discussion

4.1 Evolution of permeability characteristics under seepage-stress coupling

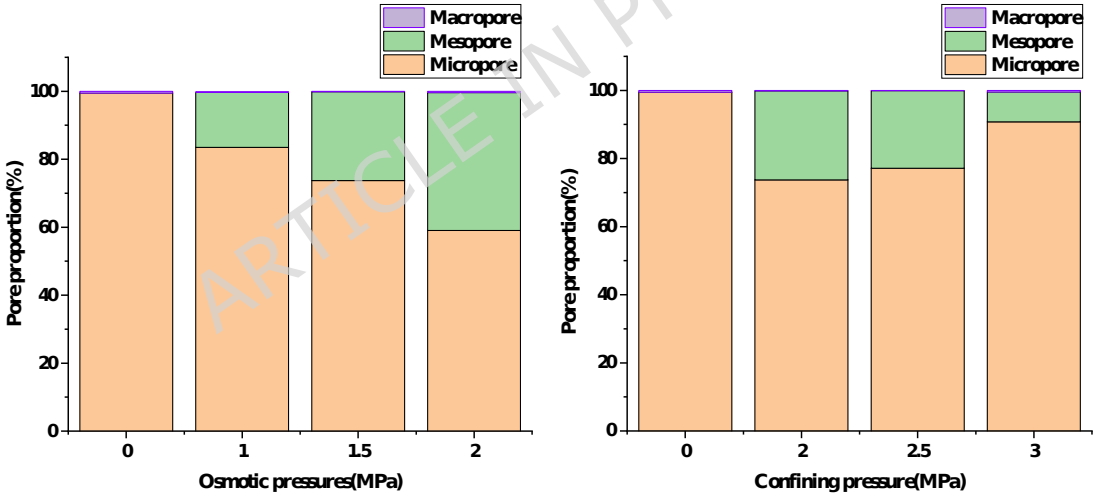

(a) (b)

Fig.10. Pore proportion of CCGB at different (a) osmotic pressures and (b) confining pressures.

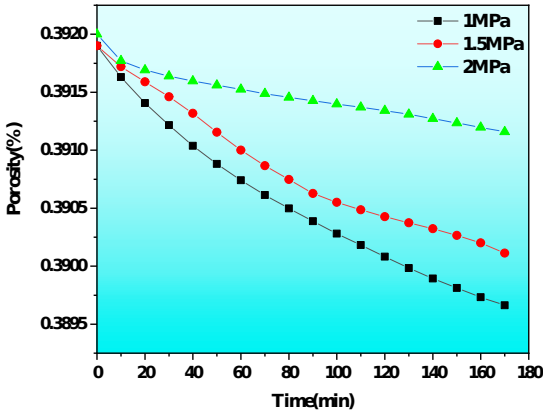

(a) Porosity

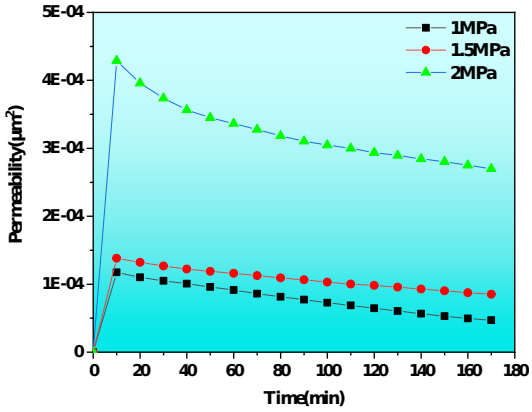

(b) Permeability

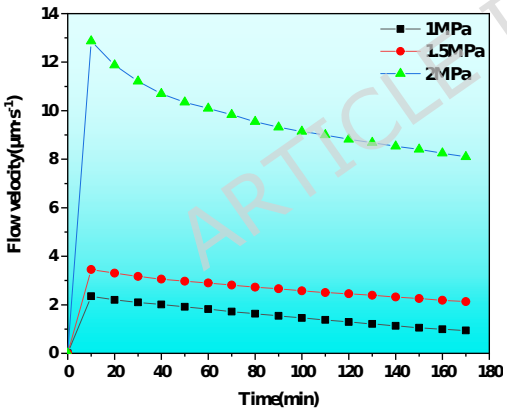

(c) Flow velocity

Fig.11. Permeability of CCGB at different osmotic pressures.

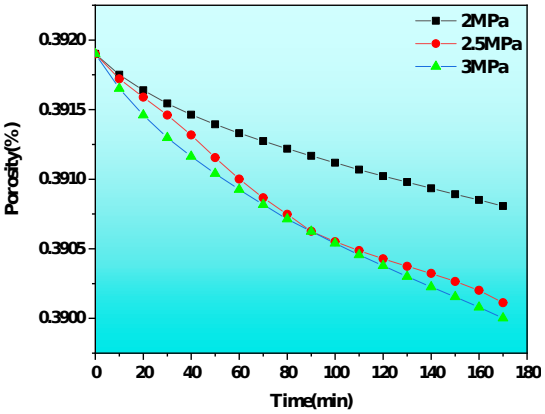

(a) Porosity

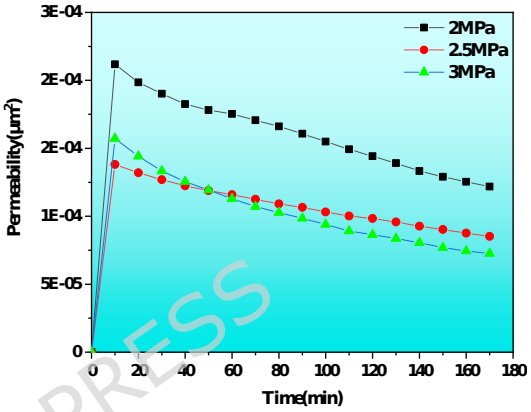

(b) Permeability

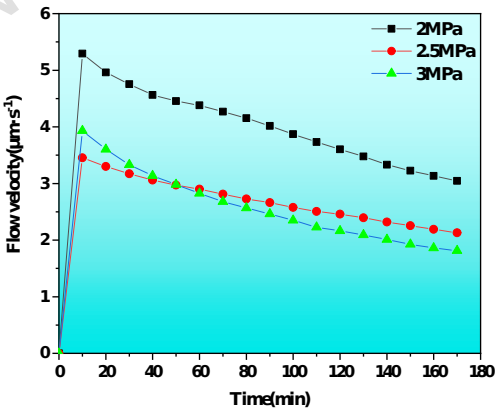

(c) Flow velocity

Fig.12. Permeability of CCGB at different confining pressures.

As shown in Fig. 10, With increasing osmotic pressure, the proportion of mesopores in the permeated specimens increased from 16.18% to 40.53%, while the proportion of micropores decreased from 83.51% to 59.06%. This is because enhanced seepage erosion

under higher osmotic pressure, with greater fluid energy, induces hydraulic fracturing of micropores to form more mesopores. With increasing confining pressure, the proportion of mesopores decreased from 26.1% to 8.8%, and the proportion of micropores increased from 73.74% to 90.75%, reflecting the volume contraction and seepage inhibition effect of confining pressure—compressing specimen volume, reducing mesopores, and inhibiting seepage impact on micropores.

Fig. 11 and 12 show the temporal characteristics of porosity under different osmotic pressures and confining pressures:

(1) 0~10 min: Porosity decreased rapidly, while flow velocity and permeability surged to peaks. This is due to initial macropores in specimens (caused by air entrainment and uneven mixing during preparation). Under high osmotic pressure, water rapidly filled pores leading to rapid saturation; meanwhile, confining pressure quickly compacted initial macropores, causing flow velocity and permeability to peak and cease growing.

(2) 10~100 min: Porosity continued to decrease but at a slowing rate (more pronounced with higher confining pressure), with flow velocity and permeability decreasing synchronously at a decelerating pace, indicating porosity dominates the evolution of seepage characteristics. During this stage, seepage parameters (porosity, permeability, flow velocity) generally decreased, with a

maximum permeability reduction amplitude of 84.4%, as sustained confining pressure compressed pores, narrowed seepage channels, and attenuated seepage performance.

(3) 100~170 min: All parameters fluctuated slightly and stabilized. Specimen volume no longer changed, with pores fully compacted and seepage channels stabilized. Under confining pressure, the structure no longer deformed or contracted, and seepage erosion did not damage the internal structure within the short test duration, leading to overall stabilization of the structure and seepage performance.

4.2 Macroscopic permeability and microstructure correlation characteristics

Due to the destructive nature of SEM and the physical constraints of the high-pressure steel chamber in SSCP tests, real-time microscopic imaging is currently impossible. Nevertheless, the acquired data remain highly valuable for characterizing and interpreting the underlying microstructural features.

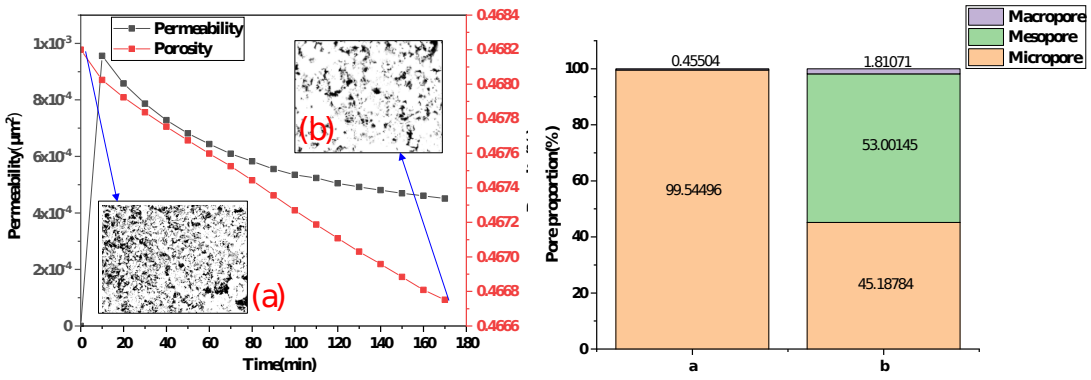

(a) 50% cement content

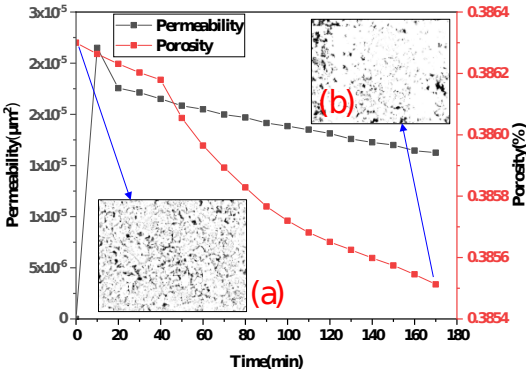

(b) 70% cement content

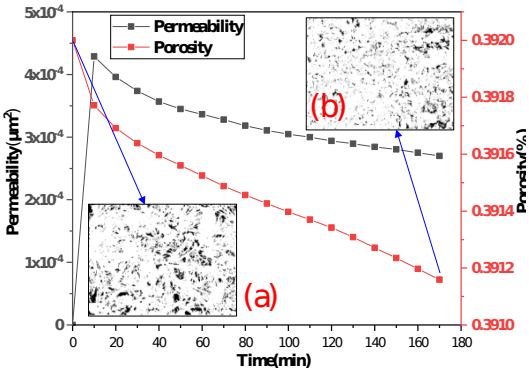

(c) 90% cement content

Fig.13. Response characteristics of permeability and porosity of CCGB under seepage-stress coupling effect

(a) 50% cement content

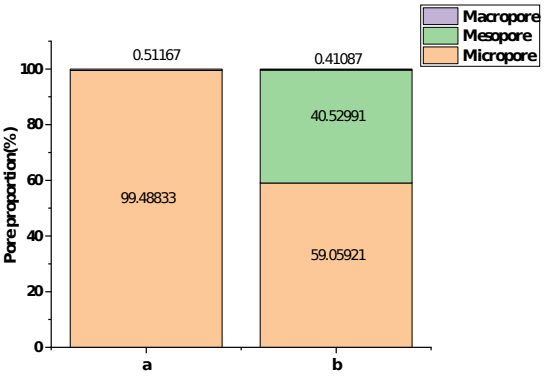

(b) 70% cement content

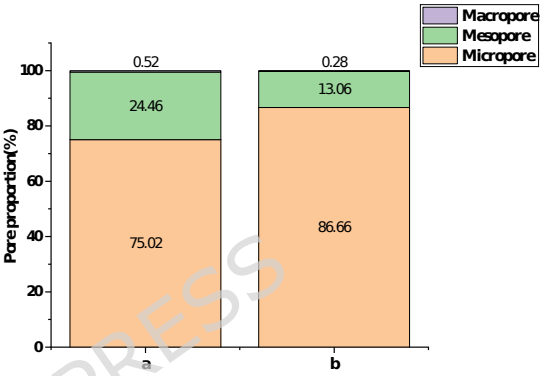

(c) 90% cement content

Fig.14. Pore size evolution diagram of CCGB with different cement contents under seepage-stress coupling effect

Fig. 13 illustrates the temporal characteristics of permeability and porosity of CCGB under seepage-stress coupling effect. They both decrease over time with similar declining patterns, with the 70% cement content specimen showing a particularly distinct behavior — permeability drops sharply at approximately 20 minutes, followed by an abrupt decrease in porosity at around 40 minutes. This phenomenon arises from the early-stage confining pressure: the connectivity of pore throats is first compressed, and the disruption

of these critical fluid flow channels causes the sudden drop in permeability. However, as CCGB is dominated by micropores, isolated pores remain uncompacted temporarily, maintaining a steady decline in porosity while accumulating deformation energy until a sudden drop in porosity occurs at 40 minutes.

Fig. 14 presents the pore size evolution of CCGB with different cement contents: after the permeability test, specimens with 50% and 70% cement content exhibit increased proportions of mesopores and macropores, accompanied by a significant decrease in micropore proportion. Although confining pressure leads to an overall reduction in porosity, seepage erosion damages the internal structure and forms seepage paths, resulting in an increased proportion of mesopores. In contrast, the 90% cement content specimen, with more hydration products and a denser structure, resists seepage erosion and prevents effective formation of flow paths, thus showing a lower mesopore proportion. This is consistent with the results in Fig. 13, where the 90% cement content specimen exhibits the lowest permeability, porosity, and proportions of mesopores and macropores.

Combined with the microscopic pore images in Fig. 13, reduced pore size leads to decreased pore connectivity. From the perspective of seepage properties, pores serve as channels for fluid flow: a lower

porosity means fewer available paths; the reduced scale of mesopores and macropores impairs the capacity of individual pores to retain and transmit fluids; and the decreased connectivity further hinders the continuous flow of fluids. With the original interconnected pore network disrupted, fluids can hardly flow smoothly between pores to form effective seepage paths, ultimately resulting in reduced permeability.

5 Conclusion

In this study, permeability tests on CCGB under seepage-stress coupling were conducted. Combined with XRD, SEM, and NMR microscopic detection techniques, the permeability characteristics evolution law of CCGB was systematically explored, and its intrinsic correlation with microstructure was revealed. The main research conclusions are as follows:

(1) The permeability and microscopic pore structure of CCGB are significantly regulated by cement content: Increasing the cement content from 50% to 70% resulted in a decrease in permeability by 1.81×10^{-4}μm^2 and a reduction in porosity by 0.076. Increasing the cement content from 70% to 90% resulted in a decrease in permeability by 2.538×10^{-4}μm^2 and a reduction in porosity by 0.006. With the increase of cement content, porosity, seepage velocity, and permeability are decreased synchronously. Under low cement content (50%, 70%), cement hydration products are insufficient, leading to a high proportion of medium-large pores between clay particles and a continuous water-conducting network; thus, seepage velocity and permeability are relatively high. Under high cement content (e.g., 90%), hydration products such as calcite and C-A-S-H gel are filled into particle gaps, making the skeleton dense and the

pores dominated by micropores. Water-conducting channels are reduced sharply, and permeability is greatly lowered.

(2) The permeability of CCGB is affected by osmotic pressure through the enhancement of seepage erosion: As osmotic pressure increases, fluid erosion is intensified, and porosity, seepage velocity, and permeability are all increased. High osmotic pressure can significantly offset the pore compaction effect of confining pressure—it not only expands the existing pore channels but also may trigger hydraulic fracturing of micropores, resulting in an increase in mesopore proportion. Under low osmotic pressure, fluid erosion force is insufficient, and pore compression is dominated by confining pressure; thus, mesopore proportion is decreased, and permeability is inhibited.

(3) Seepage in CCGB is inhibited by confining pressure through the enhancement of volume compression: With the increase of confining pressure, CCGB's volume shrinkage and seepage inhibition effects are strengthened, and porosity, seepage velocity, and permeability are all decreased. In the initial stage of seepage loading (rapid saturation stage), the regulatory role of confining pressure is prominent: Under high confining pressure (3 MPa), initial large pores are quickly compressed and closed, with porosity

decreasing by more than 15%, and the peaks of seepage velocity and permeability are significantly reduced. Under low confining pressure (2 MPa, 2.5 MPa), pore compression is slow, and initial water-conducting channels are retained for a longer time; thus, the reduction in porosity is smaller, and the peaks of seepage velocity and permeability are higher.

(4) Under seepage-stress coupling, the permeability evolution of CCGB is dominated by the “competitive balance between erosion effect and compaction effect”, with microscopic pore structure and mineral composition serving as key regulatory factors. On one hand, osmotic pressure enhances the erosion effect, increases the proportion of medium-large pores, and thereby raises porosity and permeability; confining pressure enhances the compaction effect, increases the proportion of micropores, and thereby reduces porosity and permeability. On the other hand, XRD detection indicates that the type and content of cement hydration products in CCGB affect the bonding strength between particles and the contact degree of aggregates. The higher the content of hydration products, the fewer the overhead pores between particles and the lower the porosity, which indirectly inhibits permeability and forms a “mineral composition-pore structure-permeability” linkage mechanism.

(5) Cement content classification for permeability control: (a) 90% cement for high-barrier applications (e.g., adjacent to aquifers) to form a dense, erosion-resistant matrix, effectively suppressing initial permeability peaks and ensuring environmental safety. (b) 70% cement for moderate permeability control, balancing material economy and structural stability for intermediate hydraulic demands. (c) 50% cement for low-risk zones with minimal hydrostatic pressure, providing an economical solution for non-critical areas.

Data Availability

The datasets used and analyzed during the current study are available from the corresponding author on reasonable request.

Declaration of Competing Interest

The authors declare that they have no known competing financial interests or personal relationships that could have appeared to influence the work reported in this paper.

Funding

This work was supported by the National Natural Science Foundation of China (Grant No.51604195), Supported by National Natural Science Foundation of Hubei Province (Grant No. 2018CFC818).

References

[1] Xin PH, Jiang J, Sun HW., et al. Effects of moisture content and disturbance load on seepage characteristics of weakly consolidated rock mass[J]. Frontiers in Earth Science, 2025,12: 1725348.

[2] Kong YX. Evaluation of water inrush control effect in a limestone mine in South China[J]. China Mining Magazine,2024,33(S1): 392-396,408.

[3] Chegbeleh LP, Akabzaa T, Akudago JA., et al. Investigation of critical hydraulic gradient and its application to the design and construction of bentonite-grout curtain[J]. Environmental Earth Sciences, 2019, 78(12): 370.

[4] Jemcov I. Impact assessment of grout curtain on the hydraulic behavior in karst, based on time a series analysis[J]. Environmental Earth Sciences, 2019, 78(14): 415.

[5] Gao XG, Gao F, Zhang N., et al. Numerical simulation of stress and permeability evolution in damaged coal[J]. International Journal of Non-Linear Mechanics, 2025, 168: 104953.

[6] Guo Y.X., Zhang Q.S., Xiao F., et al. Grouting rock fractures under condition of flowing water[J]. Carbonates and Evaporites, 2020, 35(3): 1-15.

[7] Jemcov I, Durovic MC. A hydraulic-hydrochemical approach to

impact assessment of a grout curtain on karst aquifer behavior[J]. Hydrogeology Journal, 2020, 29(1): 179-197.

[8] Mozafari M, MilanovićP, Jamei J. Water leakage problems at the Tangab Dam Reservoir(SW Iran), case study of the complexities of dams on karst[J]. Bulletin of Engineering Geology and the Environment, 2021, 80(10): 7989-8007.

[9] Li S.C., Liu R.T., Zhang Q.S., et al. Protection against water or mud inrush in tunnels by grouting: a review[J]. Journal of Rock Mechanics and Geotechnical Engineering, 2016, 8: 753766.

[10] Wu J, Xing KY, Guo L., et al. Seepage instability mechanism of water inrush channel in non-uniform filling-type karst tunnels under different fine particle contents[J]. Bulletin of Engineering Geology and the Environment, 2025, 85(1): 31.

[11] Yang Z, Gan L, Zhang ZL., et al. Experimental investigation on seepage characteristics of concrete with a single fracture under stress-erosion coupling effect[J]. Journal of Building Engineering, 2025, 103: 112160.

[12] Wu RY, Chen SW, Wang GB., et al. Development and application of a thermo-hydro-mechanical coupling test system for a single rock fracture[J]. Measurement, 2025, 242(Part D): 116197.

[13] Liu YX, Gao Y, Wang G., et al. Development of

experimental system for rock anisotropic seepage under true triaxial stress[J]. Geomechanics for Energy and the Environment, 2025, 42: 100677.

[14] Liu C, Liu YX, Xie ZC., et al. Experimental Study on the Dilatancy Characteristics and Permeability Evolution of Sandstone under Different Confining Pressures[J]. Sustainability, 2023, 15(20): 14795.

[15] Zhang Y, Wu X, Wu Q., et al. Investigation of Permeability Characteristics of Rock Under Confining Pressure–Fracture Coupling Conditions [J]. Rock Mechanics and Rock Engineering, 2025, 58: 7345-7361.

[16] Ma D, Wang JJ, LI ZH. Effect of particle erosion on mining-induced water inrush hazard of karst collapse pillar. Environmental Science and Pollution Research,2019,26:19719-19728

[17] Ma D, Duan HY, Zhang JX., et al. Experimental study on creep-erosion coupling mechanical properties of water inrush disaster in fractured rock mass of fault zone[J]. Chinese Journal of Rock Mechanics and Engineering, 2021, 40(09): 1751-1763.

[18] Wu JY, Feng MM, Chen, ZQ., et al. Influence of dissolution on permeability characteristics of fractured mudstone[J]. Journal of Harbin Institute of Technology, 2019, 51(2): 117-125.

[19] Wang J A, ParkHD., Fluid permeability of sedimentary rocks in a complete stress–strain process[J]. Engineering Geology, 2002, 63(3): 291-300.

[20] Nicksiar M, Martin CD., Evaluation of methods for determining crack initiation in compression tests on low-porosity rocks[J]. Rock Mechanics and Rock Engineering, 2012, 45(4): 607-617.

[21] Shu B, Zhu RJ, Tan JQ., et al. Evolution of permeability in a single granite fracture at high temperature[J]. Fuel, 2019,242: 12-22

[22] Zhang W, Wang D, Wang ZL., et al. Study on permeability evolution and damage mechanism along the EGS fracture in heat mining stage under thermal stress/cracking[J]. Geothermal Energy, 2023, 11(1): 31.

[23] Yin Q, Liu RC, Jing HW., et al. Experimental study of nonlinear flow behaviors through fractured rock samples after high-temperature exposure[J]. Rock Mechanics and Rock Engineering, 2019, 52:2963 -2983.

[24] Sun YC, Wei YF, Hu SH., et al. Study on permeability characteristics of rock mass considering nonlinear seepage in discrete fracture network[J]. Chinese Journal of Rock Mechanics and

Engineering, 2025, 44(9): 2444-2455.

[25] Zhu HX, Han LJ., et al. Experimental study on grouting seepage characteristics of single-fracture specimen under three-dimensional stress[J]. Arabian Journal of Geosciences, 2022, 15: 840.

[26] Yao N, Chen JW, Hu NY., et al. Experimental study on expansion mechanism and characteristics of expansive grout [J]. Construction and Building Materials, 2021, 268: 121574.

[27] Liu Y, Wu ZJ, Weng L., et al. Grouting diffusion characteristics in rough sandstone fracture with flowing water: Insights from NMR experimental investigation[J]. Tunnelling and Underground Space Technology, 2025, 157: 106372.

[28] Wei YX, Chai LJ, Cheng AP., et al. Experimental study on evolution of permeability characteristics of tailings stone bodies under seepage-stress coupling[J]. Metal Mine, 2025, (06): 52-62.

[29] He SY, Qian ZW, Zheng HB., et al. Study on grout seepage diffusion and fracture deformation laws in fractured rock mass based on visualized experiments[J]. Environmental Earth Sciences, 2025, 84: 574.

[30] Cao ZZ, Xiong Y, Xue Y., et al. Diffusion Evolution Rules of Grouting Slurry in Mining-induced Cracks in Overlying Strata [J]. Rock Mechanics and Rock Engineering, 2025, 58: 6493-6512.

[31] Liu, C., Zhang, X., Chen, L., et al. Investigation on the Microscopic Deterioration Characteristics of Anhydrite Rock Exposed to Freeze-Thaw Cycles[J]. Materials, 2024, 17(3), 726.